

**CO<sub>2</sub> hydrogenation to methanol over Cd<sub>4</sub>/TiO<sub>2</sub> catalyst  
Insight into multifunctional interface**

Li, G.; Meeprasert, J.; Wang, J.; Li, C.; Pidko, E.A.

**DOI**

[10.1002/cctc.202101646](https://doi.org/10.1002/cctc.202101646)

**Publication date**

2022

**Document Version**

Final published version

**Published in**

ChemCatChem

**Citation (APA)**

Li, G., Meeprasert, J., Wang, J., Li, C., & Pidko, E. A. (2022). CO<sub>2</sub> hydrogenation to methanol over Cd<sub>4</sub>/TiO<sub>2</sub> catalyst: Insight into multifunctional interface. *ChemCatChem*, 14(5), Article e202101646. <https://doi.org/10.1002/cctc.202101646>

**Important note**

To cite this publication, please use the final published version (if applicable).  
Please check the document version above.

**Copyright**

Other than for strictly personal use, it is not permitted to download, forward or distribute the text or part of it, without the consent of the author(s) and/or copyright holder(s), unless the work is under an open content license such as Creative Commons.

**Takedown policy**

Please contact us and provide details if you believe this document breaches copyrights.  
We will remove access to the work immediately and investigate your claim.



# CO<sub>2</sub> Hydrogenation to Methanol over Cd<sub>4</sub>/TiO<sub>2</sub> Catalyst: Insight into Multifunctional Interface

Guanna Li,<sup>\*[a, b]</sup> Jittima Meeprasert,<sup>[c]</sup> Jijie Wang,<sup>[d]</sup> Can Li,<sup>[d]</sup> and Evgeny A. Pidko<sup>\*[c]</sup>

Supported metal catalysts have shown to be efficient for CO<sub>2</sub> conversion due to their multifunctionality and high stability. Herein, we have combined density functional theory calculations with microkinetic modeling to investigate the catalytic reaction mechanisms of CO<sub>2</sub> hydrogenation to CH<sub>3</sub>OH over a recently reported catalyst of Cd<sub>4</sub>/TiO<sub>2</sub>. Calculations reveal that the metal-oxide interface is the active center for CO<sub>2</sub> hydrogenation and methanol formation via the formate pathway

dominates over the reverse water-gas shift (RWGS) pathway. Microkinetic modeling demonstrated that formate species on the surface of Cd<sub>4</sub>/TiO<sub>2</sub> is the relevant intermediate for the production of CH<sub>3</sub>OH, and CH<sub>2</sub>O<sup>#</sup> formation is the rate-determining step. These findings demonstrate the crucial role of the Cd-TiO<sub>2</sub> interface for controlling the CO<sub>2</sub> reduction reactivity and CH<sub>3</sub>OH selectivity.

## Introduction

The increase of CO<sub>2</sub> concentration in the atmosphere is one of the major factors in global climate change. CO<sub>2</sub> capture and valorization have been considered as promising strategies to mitigate this problem.<sup>[1]</sup> Using CO<sub>2</sub> as a feedstock to produce valuable chemicals not only can help to decrease dramatically

the amount of CO<sub>2</sub> emitted into the atmosphere but also provide economic benefits.<sup>[1b,2]</sup> A large number of value-added chemicals can be produced from CO<sub>2</sub> via platform molecules such as CO, CH<sub>4</sub>, and CH<sub>3</sub>OH.<sup>[3]</sup> Among these, CH<sub>3</sub>OH is highly desirable because it is an important fuel as well as a starting feedstock for the production of more valuable chemical compounds.<sup>[4]</sup> Recently, two different approaches for CO<sub>2</sub> hydrogenation to CH<sub>3</sub>OH have received a lot of attention: (1) electrochemical reduction and (2) thermochemical reduction.<sup>[5]</sup> The electrochemical CO<sub>2</sub> reduction offers the advantage that product distribution can be controlled by adjusting electrolyte, electrocatalyst, and applied voltage.<sup>[6]</sup> However, the selectivity, energetic efficiency, electrode lifetime restrict to its large-scale applications.<sup>[6c,d]</sup> Therefore, using the thermochemical approach to synthesize CH<sub>3</sub>OH from CO<sub>2</sub> hydrogenation is more practical for potential industrial applications compared to the alternative electrochemical CO<sub>2</sub> reduction. It offers an opportunity for the development of sustainable technologies and environmentally benign chemical processes since H<sub>2</sub> which is a reducing agent can readily be obtained from renewable energy resources.<sup>[1a,2]</sup>


Many studies have been devoted to creating new tailor-made CO<sub>2</sub> conversion catalysts with improved activity and selectivity to methanol, of which Cu/ZnO/Al<sub>2</sub>O<sub>3</sub> catalyst has been industrialized.<sup>[7]</sup> However, the disadvantages of low CH<sub>3</sub>OH selectivity and the sintering of Cu and ZnO motivated the development of new Cu-based catalysts such as Cu/ZnO,<sup>[8]</sup> Cu/ZrO<sub>2</sub>,<sup>[9]</sup> and Cu/CeO<sub>2</sub>.<sup>[10]</sup> In these catalytic systems, it was found that H<sub>2</sub> molecule is dissociated at the Cu site and CO<sub>2</sub> is activated at the oxide surface, while the interface between Cu and metal oxide supports plays a crucial role for stabilization of the reaction intermediate for CH<sub>3</sub>OH formation.<sup>[9]</sup> Besides Cu-based catalysts, various other materials have also been reported as promising catalysts for CO<sub>2</sub> hydrogenation to CH<sub>3</sub>OH. For instance, Au,<sup>[11]</sup> Pd<sup>[12]</sup>, Re,<sup>[13]</sup> ZnO<sup>[14]</sup> and In<sub>2</sub>O<sub>3</sub><sup>[15]</sup> supported on oxides were reported to be active toward the production of CH<sub>3</sub>OH under moderate conditions. Although many different types of catalysts have been reported, all of the active sites


[a] Dr. G. Li  
Biobased Chemistry and Technology  
Wageningen University & Research  
Bornse Weiland 9, 6708WG Wageningen  
(The Netherlands)


[b] Dr. G. Li  
Laboratory of Organic Chemistry  
Wageningen University & Research, Stippeneng 4, 6708WE Wageningen,  
(The Netherlands)  
E-mail: guanna.li@wur.nl  
Homepage: <https://www.wur.nl/en/Research-Results/Chair-groups/Agrotechnology-and-Food-Sciences/Laboratory-of-Organic-Chemistry/Research/Theoretical-Surface-Chemistry.htm>

[c] J. Meeprasert, Prof. E. A. Pidko  
Inorganic Systems Engineering  
Department of Chemical Engineering  
Delft University of Technology, Van der Maasweg 9 2629 HZ Delft  
(The Netherlands)  
E-mail: E.A.Pidko@tudelft.nl  
Homepage: <https://www.tudelft.nl/tnw/over-faculteit/afdelingen/chemical-engineering/principal-scientists/evgeny-pidko/evgeny-pidko>

[d] Prof. J. Wang, Prof. C. Li  
State Key Laboratory of Catalysis  
Dalian Institute of Chemical Physics  
Chinese Academy of Sciences  
457 Zhongshan Road, Dalian 116023  
(P. R. China)

 Supporting information for this article is available on the WWW under <https://doi.org/10.1002/cctc.202101646>

 This publication is part of a Special Collection on "Supported Nanoparticles and Single-Atoms for Catalysis: Energy and Environmental Applications". Please check the ChemCatChem homepage for more articles in the collection.

 © 2022 The Authors. ChemCatChem published by Wiley-VCH GmbH. This is an open access article under the terms of the Creative Commons Attribution License, which permits use, distribution and reproduction in any medium, provided the original work is properly cited.

involved in the reaction have a common feature of multifunctionality in nature. An efficient cooperation between active sites of different catalytic natures coupled in one heterogeneous catalyst plays a key role for eventual selective CH<sub>3</sub>OH formation.

Regarding the reaction mechanism, typically, two different reaction pathways have been proposed for the hydrogenation of CO<sub>2</sub> to CH<sub>3</sub>OH: (1) the reverse water-gas shift (RWGS) pathway, and (2) the formate pathway. In the RWGS reaction, CO<sub>2</sub> is hydrogenated to form CO\* intermediate which is then further hydrogenated to form CH<sub>3</sub>OH. For the formate pathway, CH<sub>3</sub>OH is produced via the formate (HCOO\*) intermediate.<sup>[16]</sup> Most studies have suggested that the formate pathway is preferred over the RWGS pathway.<sup>[7b,12a,17]</sup> The main reason is that the binding strength of CO\* intermediate on these catalysts is quite weak, leading to the desorption of CO to the gas phase. However, on some other catalysts such as Cu/TiO<sub>2</sub>, Cu/ZrO<sub>2</sub>, and Cu/CeO<sub>x</sub>, CH<sub>3</sub>OH was produced through CO\* intermediate due to the strong enough interaction between CO\* and catalyst.<sup>[9b,10]</sup> Therefore, the specific reaction pathway dominating methanol formation is system-dependent and should be investigated individually.

Recently we have investigated CO<sub>2</sub> conversion to CH<sub>3</sub>OH on Cd/TiO<sub>2</sub> and CdTiO<sub>3</sub> catalysts by a combination of experimental and computational studies.<sup>[18]</sup> It was found that Cd/TiO<sub>2</sub> catalyst exhibits a much higher catalytic CO<sub>2</sub> hydrogenation activity than the CdTiO<sub>3</sub> mixed oxide. To further identify the detailed reaction mechanism catalyzed by Cd/TiO<sub>2</sub> and clarify the functionalities of different types of active sites in this system, we constructed a Cd/TiO<sub>2</sub> model catalyst and investigated its catalytic activity towards CO<sub>2</sub> conversion to methanol with H<sub>2</sub> as a reductant. The key objective of this study is to explore the multiple-site cooperation effects on the catalyst reactivity by combining DFT calculation with microkinetic modeling.

## Results and Discussion

### Cd<sub>4</sub>/TiO<sub>2</sub> Model rationalization

A cluster containing 4 Cd atoms (Cd<sub>4</sub>) was selected as representative of the supported Cd nanoparticles on the TiO<sub>2</sub> surface since it was reported as the smallest Cd cluster featuring a magic number of Cd atoms. In order to model the Cd<sub>4</sub>/TiO<sub>2</sub> catalyst, two possible configurations of isolated Cd<sub>4</sub> cluster, i.e., a tetrahedron (T<sub>d</sub>) and planar rhombus (C<sub>2v</sub>)<sup>[28]</sup> were firstly optimized in the vacuum by using a large unit cell of 15×15×15 Å (Figure S1 in the supporting information). Then the so-obtained Cd<sub>4</sub> clusters were deposited and optimized on the (101) surface of anatase TiO<sub>2</sub>. It is found that the most stable configuration of the supported Cd<sub>4</sub> cluster on the (101) TiO<sub>2</sub> surface is a deformed planar geometry even though the tetrahedron is more stable in the gas phase. As shown in Figure 1, the Cd<sub>4</sub> (C<sub>2v</sub>) cluster is slightly distorted upon the adsorption with one of the Cd atoms lying above the plane of the other three. The adsorption energy of Cd<sub>4</sub> over the surface is calculated to be −1.05 eV indicating a strong interaction

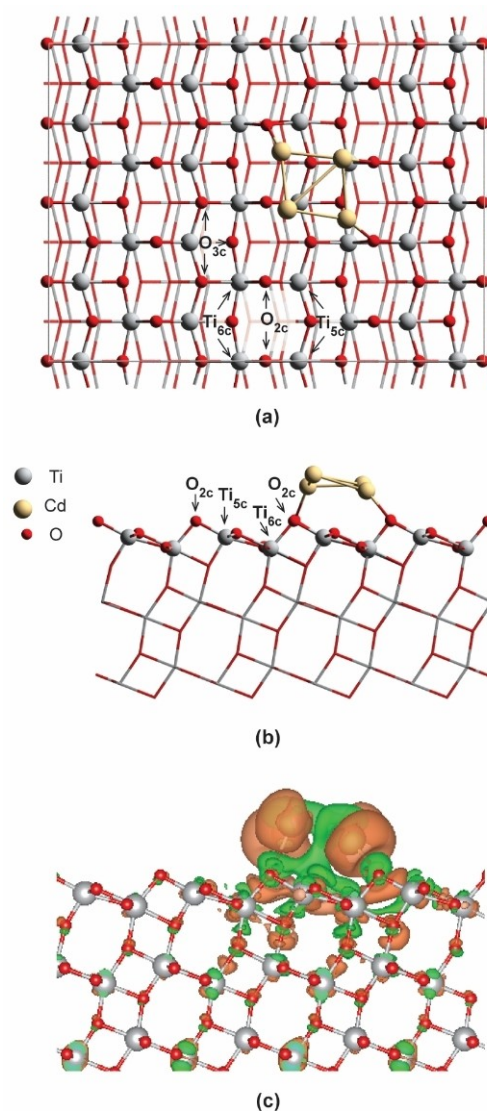


**Figure 1.** (a) Top view and (b) side view of Cd<sub>4</sub>/TiO<sub>2</sub>(101) slab model. The O<sub>2c</sub> and O<sub>3c</sub> are twofold coordinated and threefold coordinated oxygen atoms, and the Ti<sub>5c</sub> and Ti<sub>6c</sub> are fivefold coordinated and sixfold coordinated titanium atoms on the surface of TiO<sub>2</sub>, respectively. (c) The electron density difference plots upon the adsorption of Cd<sub>4</sub> cluster on TiO<sub>2</sub> surface. The orange and green regions represent electrons depletion and accumulation respectively (isosurface value = 0.05 e/Bohr<sup>3</sup>).

between the metal cluster and the support of TiO<sub>2</sub>. Bader charge analysis demonstrates that the entire Cd<sub>4</sub> cluster is +1.48|e| charged, which indicates that the electrons are transferred from Cd<sub>4</sub> cluster to TiO<sub>2</sub> surface through metal-support interaction.

### H<sub>2</sub> dissociation and H spillover

Many studies have proposed that activation and dissociation of an H<sub>2</sub> molecule take place at the metal-oxide interface.<sup>[29]</sup> In this work, six possible active sites of Cd<sub>4</sub>/TiO<sub>2</sub> catalyst for the activation and dissociation of H<sub>2</sub> molecule were systematically

studied. As shown in Figure 2, site A is on top of the supported  $\text{Cd}_4$  cluster. Site B, C and D are at the interface of  $\text{Cd}_4/\text{TiO}_2$  ( $\text{Cd}-\text{O}_{2c}$ ). Site E is located between two nearest  $\text{O}_{2c}$  atoms and site F is on top of bridging  $\text{Ti}_{5c}$  and  $\text{O}_{2c}$  atoms of  $\text{TiO}_2$  surface. From Figure 2 it can be seen that heterolytic  $\text{H}_2$  dissociation at the interface of  $\text{Cd}/\text{TiO}_2$  is more preferable than the other sites. Among all interface sites considered,  $\text{H}_2$  dissociation over site C has the lowest activation barrier (0.39 eV). Homolytic dissociation of  $\text{H}_2$  molecule over site A needs to overcome an activation barrier of 0.88 eV and generates two hydrides on the supported  $\text{Cd}_4$  cluster. On the  $\text{TiO}_2$  surface, both homolytic (site E) and heterolytic dissociation pathways (site F) exhibit very high activation barriers (1.74 and 2.25 eV) indicating that  $\text{TiO}_2$  surface site is inactive for  $\text{H}_2$  activation. This is in agreement with a previous theoretical study of  $\text{H}_2$  dissociation on  $\text{TiO}_2$  surfaces.<sup>[30]</sup>

After we figured out the most favorable active site for  $\text{H}_2$  dissociation, the spillover process of the so-formed  $\text{H}^*$  on the surface of the  $\text{Cd}_4/\text{TiO}_2$  is further studied. As shown in Figure S2, the migration of the  $\text{H}^*$  generated by  $\text{H}_2$  dissociation at the interface (site C) from  $\text{O}_{2c}$  site to its neighboring  $\text{O}_{3c}$  site has an activation barrier of 0.73 eV. The other  $\text{H}^*$  species on the  $\text{Cd}_4$  cluster can also spillover to the surface of  $\text{TiO}_2$  with an activation barrier of 0.71 eV.  $\text{H}^*$  on  $\text{O}_{3c}$  site can also hop to another  $\text{O}_{2c}$  site next to it by overcoming a barrier of only 0.42 eV. The overall reaction is slightly endothermic. These results indicate that the activated  $\text{H}^*$  on the surface of the  $\text{Cd}_4/\text{TiO}_2$  catalyst is rather dynamic and hydrogen migrations among different surface sites is thermodynamically and kinetically easy processes.

## $\text{CO}_2$ hydrogenation to $\text{HCOOH}$ and $\text{CO}$

In this section, the hydrogenation of  $\text{CO}_2$  on  $\text{Cd}_4/\text{TiO}_2$  catalyst will be discussed. Two main reaction pathways of  $\text{CO}_2$  hydro-

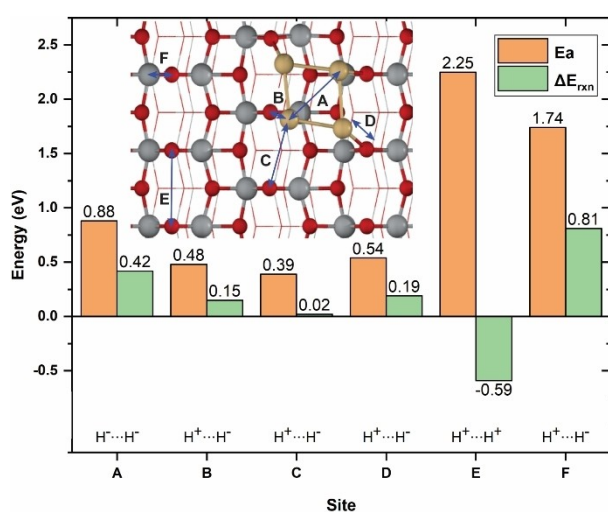


**Figure 2.** Activation energy ( $E_a$ ) and reaction energy ( $\Delta E_{rxn}$ ) for  $\text{H}_2$  dissociation at all possible active sites of  $\text{Cd}_4/\text{TiO}_2$  catalyst.

genation which have been intensively debated in the literature were studied: (1) methanol formation via the intermediate of  $\text{HCOOH}^*$ , and (2) methanol formation via the reversed water-gas shift (RWGS) pathway with  $\text{CO}$  as an intermediate. Noted that the species with asterisk (\*) and hash sign (#) are species that interact with  $\text{TiO}_2$  surface and  $\text{Cd}_4$  cluster of the  $\text{Cd}_4/\text{TiO}_2$  catalyst, respectively.

## Formate pathway

The reaction mechanisms of  $\text{CO}_2$  hydrogenation to formate ( $\text{HCOO}^*$ ) and formic acid ( $\text{HCOOH}^*$ ) are shown in Figure 3. After heterolytic dissociation of  $\text{H}_2$  at the interface of  $\text{Cd}_4/\text{TiO}_2$ , a hydride coordinated to  $\text{Cd}$  ( $\text{H}^\#$ ) and a proton bonded to  $\text{O}_{2c}$  site ( $\text{H}^*$ ) are produced.  $\text{CO}_2$  is adsorbed over the  $\text{Ti}_{5c}$  site nearby both  $\text{H}^*$  and  $\text{H}^\#$  species. The adsorption energy is calculated to be  $-0.14$  eV. Then  $\text{CO}_2$  can be hydrogenated by the transfer of  $\text{H}^\#$  from  $\text{Cd}_4$  cluster to the C atom of  $\text{CO}_2$  forming formate intermediate of  $\text{HCOO}^*$ . The activation barrier for this step is only 0.26 eV. Further protonation of  $\text{HCOO}^*$  to form formic acid ( $\text{HCOOH}^*$ ) can be realized via two different reaction routes, either by protonation of monodentate  $\text{HCOO}^*$  intermediate to form *cis*- $\text{HCOOH}^*$  (gray line in Figure 3), or protonation of bidentate  $\text{HCOO}^{\#}$  intermediate which can be formed by structure rearrangement to form *trans*- $\text{HCOOH}^{\#}$  (orange line in Figure 3). The activation barriers of proton transfer for both routes are relatively low (0.22 and 0.41 eV), however, the configurational transformation of  $\text{HCOO}^*$  from monodentate coordination to bidentate coordination with both  $\text{Ti}_{5c}$  and  $\text{Cd}$  before protonation reaction is dramatically favorable. Another possible pathway for  $\text{HCOOH}^*$  formation is also identified with a small activation barrier of 0.15 eV, the so-called concerted reaction mechanism with  $\text{CO}_2$  hydrogenation by both  $\text{H}^*$  and  $\text{H}^\#$  in one step (green line in Figure 3).

## RWGS pathway

The RWGS reaction mechanism is initiated by  $\text{CO}_2$  hydrogenation to first form carboxylate intermediate ( $\text{HOCO}^\#$ ), from which  $\text{CO}$  is produced and can be further converted into methanol by continuous hydrogenation reactions. As shown in Figure 4, the reaction starts with the adsorption of  $\text{CO}_2$  at the perimeter site of  $\text{Cd}_4$  cluster after hydrogen spillover process. Then, the  $\text{CO}_2$  can be protonated by the  $\text{H}^*$  on  $\text{TiO}_2$  surface forming  $\text{HOCO}^\#$ . It is found that this reaction cannot occur directly due to the long distance between  $\text{CO}_2$  and  $\text{H}^*$  (4.93 Å). However, it can proceed by the assist of an  $\text{H}_2\text{O}$  molecule which acts as a proton shuttle between  $\text{H}^*$  and  $\text{CO}_2$  (blue line in Figure 4). The activation energy in this case is calculated to be 0.42 eV indicating that this process is feasible. Subsequent hydrogenation of the  $\text{HOCO}^\#$  intermediate at its terminal OH group with the breaking of C–O bond produces  $\text{CO}^\#$  and  $\text{H}_2\text{O}^*$ . This process requires overcome an activation barrier of 0.35 eV. Finally,  $\text{CO}$  and  $\text{H}_2\text{O}$  can be desorbed from the catalyst with desorption barriers of 0.13 and 0.19 eV, respectively.

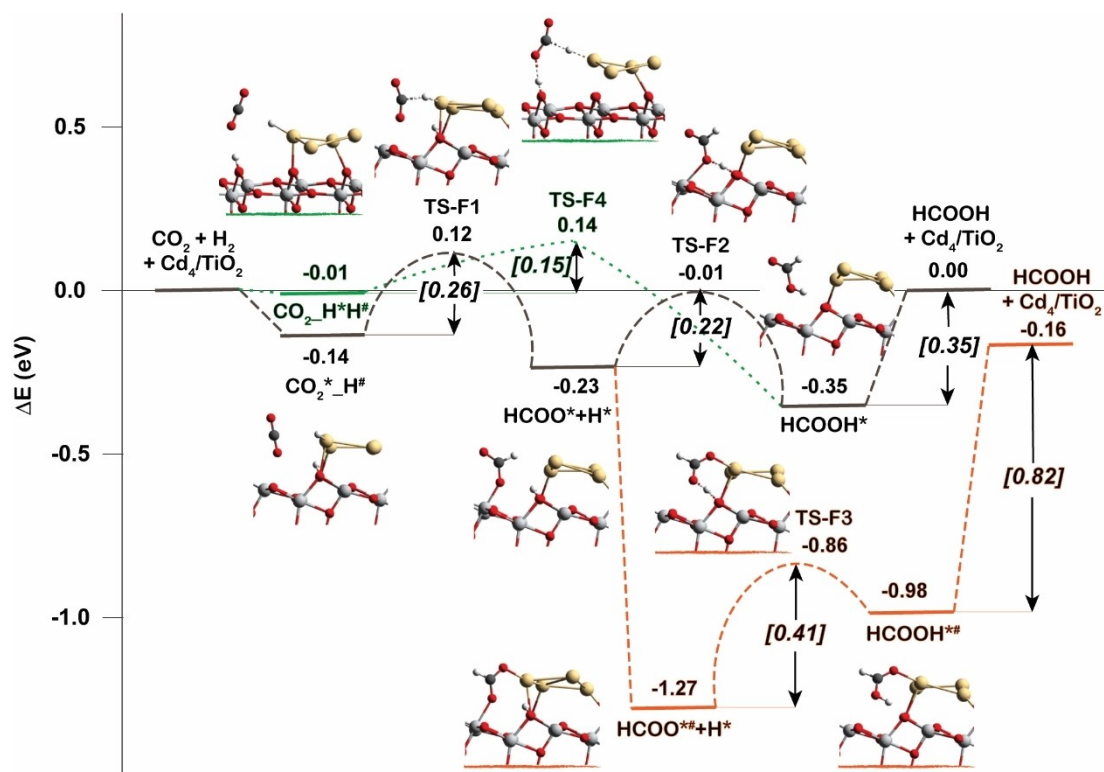


**Figure 3.** Reaction energy profiles for the  $\text{CO}_2$  hydrogenation to  $\text{HCOOH}^*$  on  $\text{Cd}_4/\text{TiO}_2$  catalyst. Green line is the concerted pathway. Gray line is the stepwise pathway via monodentate  $\text{HCOO}^*$ . Orange line is the stepwise pathway via bidentate  $\text{HCOO}^{**}$ . The species with asterisk (\*) and hash sign (#) are species that interact with  $\text{TiO}_2$  surface and  $\text{Cd}_4$  cluster of the  $\text{Cd}_4/\text{TiO}_2$  catalyst, respectively.

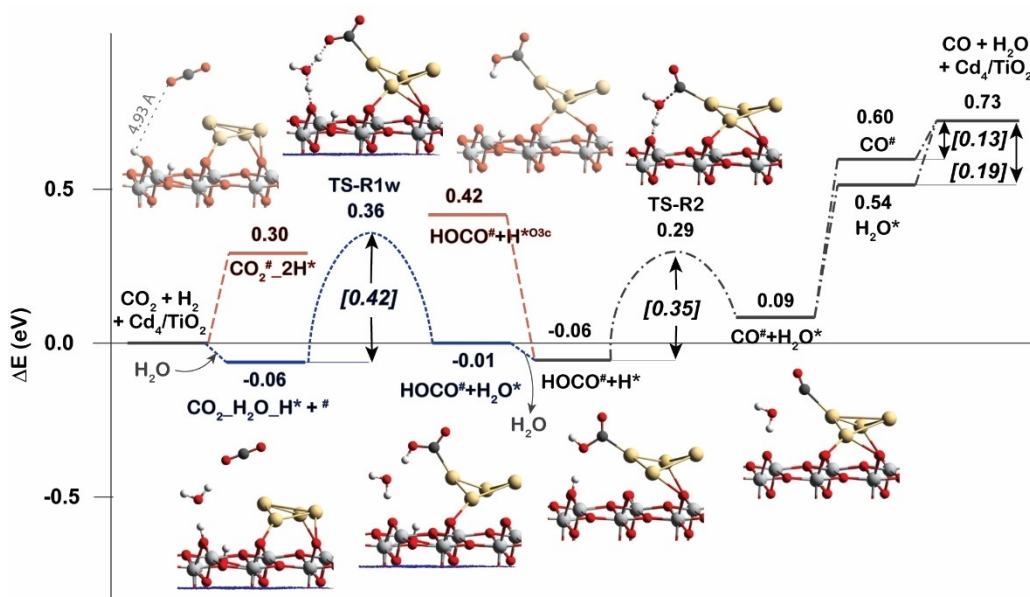


**Figure 4.** Reaction energy profiles for the  $\text{CO}_2$  hydrogenation to CO on  $\text{Cd}_4/\text{TiO}_2$  catalyst (RWGS pathway). Blue line is the reaction with the assist of  $\text{H}_2\text{O}$  molecule.

Due to the unfavorable adsorption of  $\text{CO}_2$  on the supported  $\text{Cd}_4$  cluster, we also explored the  $\text{CO}_2$  adsorption on a separate  $\text{TiO}_2$  surface site without interaction with the  $\text{Cd}_4$  cluster. The

mechanisms of RWGS reaction on the  $\text{TiO}_2$  surface are shown in Figure 5. In this case this reaction starts with the adsorption of  $\text{CO}_2$  on the  $\text{TiO}_2$  surface after hydrogen spillover process. The

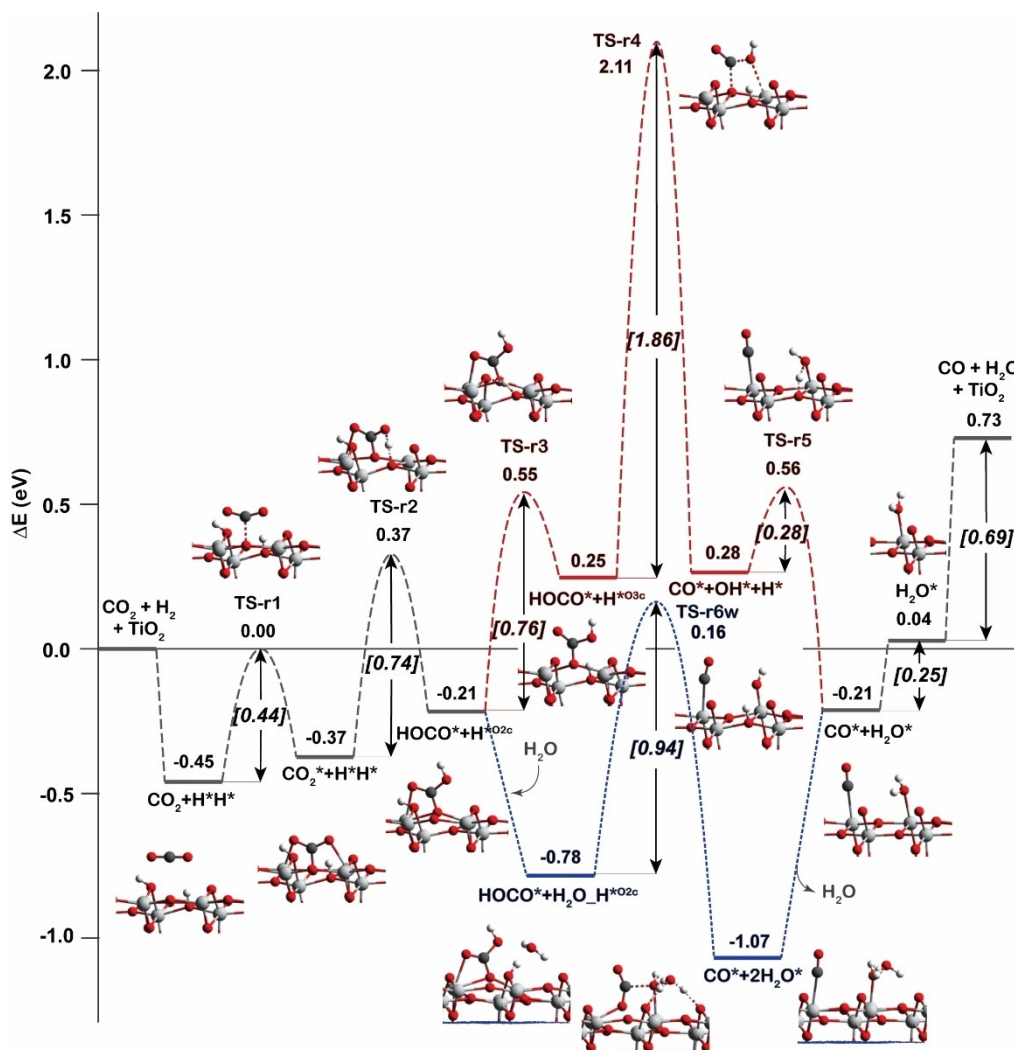


**Figure 5.** Reaction energy profiles for the CO<sub>2</sub> hydrogenation to CO on clean TiO<sub>2</sub> surface (RWGS pathway). Blue line is the reaction with the assist of H<sub>2</sub>O molecule.

adsorption energy of CO<sub>2</sub> is calculated to be  $-0.45$  eV which is relatively stronger than that on supported Cd<sub>4</sub> cluster. The bent CO<sub>2</sub> geometry can be formed on the TiO<sub>2</sub> surface with an activation barrier of 0.44 eV. Then the adsorbed CO<sub>2</sub>\* is directly hydrogenated to form HOCO\* without the H<sub>2</sub>O mediator. The activation energy for this step is calculated to be 0.74 eV. The diffusion of the second H\* to the O<sub>3c</sub> site close to the OH group of HOCO\* needs overcome an activation barrier of 0.76 eV. After that, the cleavage of the C–O bond of HOCO\* intermediate to generate CO\* and OH\* species on the TiO<sub>2</sub> surface is rather difficult with an activation barrier of 1.86 eV. However, the presence of H<sub>2</sub>O molecule can again decrease this activation barrier to 0.94 eV with C–O bonding breaking and OH group hydrogenation occurring simultaneously.

It is found that H<sub>2</sub>O molecule plays an important role as a proton shuttle to promote the most difficult reaction steps during the RWGS reactions taking place at both interface and TiO<sub>2</sub> surface of Cd<sub>4</sub>/TiO<sub>2</sub> catalyst. The hydrogenation reaction of CO<sub>2</sub> is the most difficult step for the reaction occurred at the

interface while the C–O bond cleavage of HOCO\* carboxylate intermediate is found to be the most difficult step for the reaction occurred at the TiO<sub>2</sub> surface. The highest activation energy of the RWGS reaction that occurs at the interface of Cd<sub>4</sub> and TiO<sub>2</sub> surface (TS-R1w) is about two times lower than that of the other reaction route on the TiO<sub>2</sub> surface (TS-r6w). Therefore, it is concluded that the most preferable active site for the RWGS reaction is the interface of Cd<sub>4</sub>/TiO<sub>2</sub> catalyst. Therefore, in the next section, the discussion of CH<sub>3</sub>OH formation via CO\* will only focus on the reaction route at the interface.

### CH<sub>3</sub>OH formation

In this section, we will discuss the reaction mechanism of CH<sub>3</sub>OH formation from HCOOH\* as well as CO\* intermediates generated from the formate and the RWGS reaction pathways. The results are shown in Figure 6. Totally 4 elementary hydrogenation reaction steps are involved for CH<sub>3</sub>OH formation from

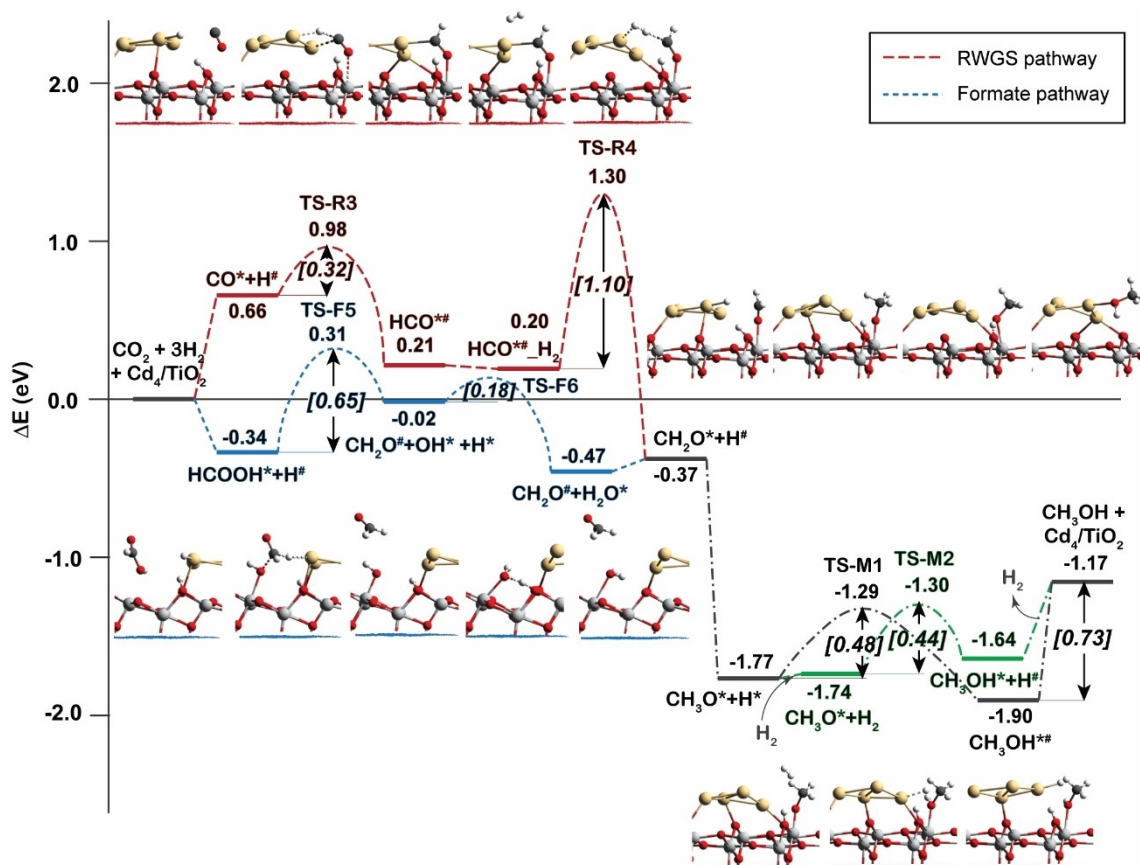


Figure 6. Reaction energy profiles for the production of  $\text{CH}_3\text{OH}$  from CO and HCOOH.

CO i.e.  $\text{CO}^* \rightarrow \text{HCO}^{\#}$ ,  $\text{HCO}^{\#} \rightarrow \text{CH}_2\text{O}^*$ ,  $\text{CH}_2\text{O}^* \rightarrow \text{CH}_3\text{O}^*$  and  $\text{CH}_3\text{O}^* \rightarrow \text{CH}_3\text{OH}$ . The activation barrier for CO hydrogenation to form  $\text{HCO}^{\#}$  is 0.32 eV by  $\text{H}^{\#}$  on  $\text{Cd}_4$  cluster. The next step of dissociative adsorption of  $\text{H}_2$  on top of  $\text{HCO}^{\#}$  intermediate generating  $\text{CH}_2\text{O}^*$  and  $\text{H}^{\#}$  species has an activation barrier of 1.10 eV. Subsequent  $\text{CH}_3\text{O}^*$  formation by  $\text{CH}_2\text{O}^*$  hydrogenation is a barrierless process with a reaction energy of  $-1.40$  eV. Finally, the  $\text{CH}_3\text{OH}$  is formed by hydrogenation of  $\text{CH}_3\text{O}^*$  intermediate with the activation barrier of 0.48 eV. In addition,  $\text{CH}_3\text{OH}$  can be produced by the hydrogenolysis of  $\text{CH}_3\text{O}^*$  (green line in Figure 6). The activation energy of this step is only 0.04 eV lower than that of the  $\text{CH}_3\text{O}^*$  hydrogenation step. These results imply that both  $\text{CH}_3\text{O}^*$  hydrogenolysis and  $\text{CH}_3\text{O}^*$  hydrogenation coexist in the formation of  $\text{CH}_3\text{OH}$ .

Alternatively,  $\text{CH}_3\text{OH}$  can also be formed from  $\text{HCOOH}^*$  (blue line in Figure 6). The initial step is the hydrogenation of  $\text{HCOOH}^*$  to produce formaldehyde ( $\text{CH}_2\text{O}^{\#}$ ) and an  $\text{OH}^*$  species ( $\text{CH}_2\text{O}^{\#} + \text{OH}^* + \text{H}^*$ ). The activation energy of this step is calculated to be 0.65 eV. Then, the  $\text{OH}^*$  is protonated to form  $\text{H}_2\text{O}$  and regenerate a vacant interfacial active site on the surface. In the next step, after another  $\text{H}_2$  molecule is dissociated at the interface, the  $\text{CH}_3\text{OH}$  can be formed by two successive hydrogenation steps from  $\text{CH}_2\text{O}^*$ , which is the same process as the reactions via the RWGS pathway.

To summarize, Figure 7 gives a schematical representation of the whole DFT reaction mechanism identified in this work, and the whole reaction pathways of  $\text{CO}_2$  hydrogenation to  $\text{CH}_3\text{OH}$  on  $\text{Cd}_4/\text{TiO}_2$  catalyst is shown in Figure S4. It can be seen that the formate pathway dominates over the RWGS pathway for the production of  $\text{CH}_3\text{OH}$  from  $\text{CO}_2$  and  $\text{H}_2$ . The formation of  $\text{CH}_2\text{O}^*$  intermediate is found to be the most difficult reaction step for  $\text{CH}_3\text{OH}$  production from both RWGS and formate reaction routes.

### Microkinetic modeling

All considered elementary steps of the  $\text{CO}_2$  hydrogenation to  $\text{CH}_3\text{OH}$  on  $\text{Cd}_4/\text{TiO}_2$  catalyst, and corresponding activation energies are listed in Table 1. The MKM is performed using a dual-site model representing  $\text{TiO}_2$  ( $^*$ ) and  $\text{Cd}$  ( $^{\#}$ ) sites on  $\text{Cd}_4/\text{TiO}_2$  catalyst, respectively. The ratio between the number of  $^*$  and  $^{\#}$  sites is 0.5:0.5. The reaction rate, surface coverages, and degree of rate control (DRC) are calculated under the following steady-state reaction conditions: total pressure = 2 MPa.,  $\text{H}_2/\text{CO}_2 = 3:1$ , temperature = 270–310 °C. The apparent activation energy ( $E_{\text{app}}$ ) is determined from the slope of the Arrhenius plot, as shown in Figure 8a. The  $E_{\text{app}}$  for the  $\text{CH}_3\text{OH}$  formation is calculated to be 1.46 eV (141.0 kJ/mol), while that for the CO

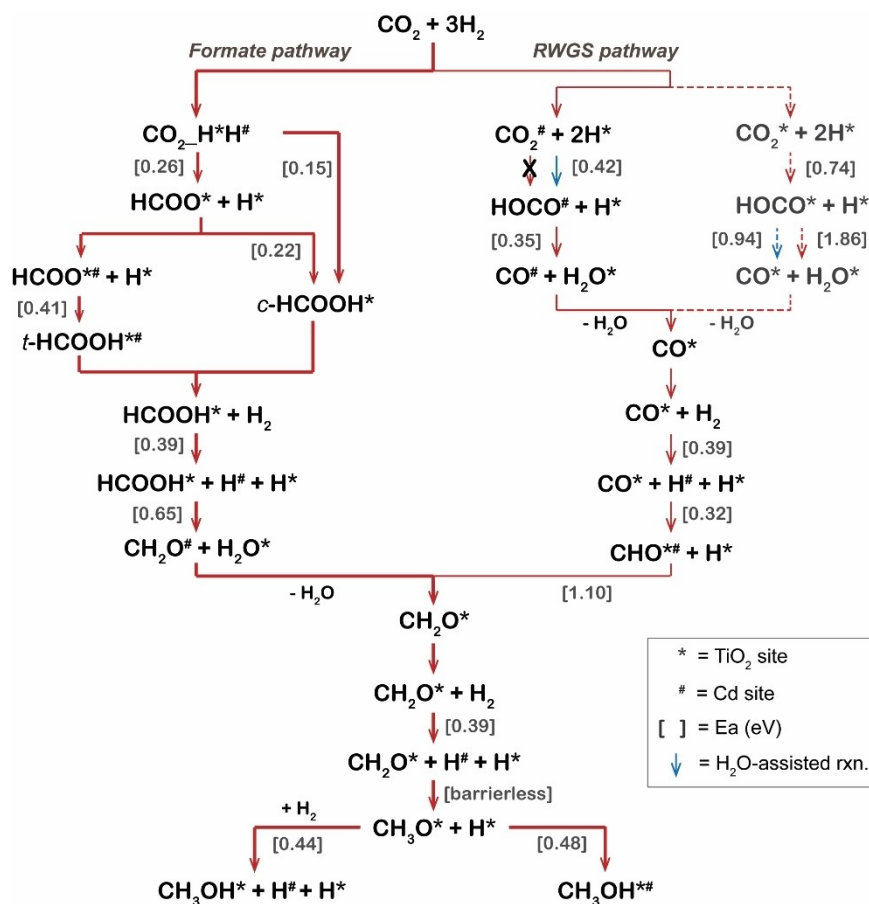


**Figure 7.** A schematic representation of the whole reaction mechanism for CO<sub>2</sub> hydrogenation to CH<sub>3</sub>OH on Cd<sub>4</sub>/TiO<sub>2</sub> catalyst. Numbers in parenthesis represent activation energies in eV. Solid lines and dash lines represent reaction that occurs at the interface and TiO<sub>2</sub> surface, respectively.

formation is much higher, 4.10 eV (395.4 kJ/mol). This agrees with the experiment that the Cd/TiO<sub>2</sub> catalyst exhibits high CH<sub>3</sub>OH selectivity (70%).<sup>[18]</sup> These results also indicate that the reaction rate of products increases with the increasing of reaction temperature.

Figure 8b shows that the HCOO\*<sup>#</sup> has the highest surface coverage ( $\sigma \approx 0.5$ ), indicating the formation of this intermediate is the resting state of the overall reaction. This result is consistent with the experimental in-situ IR observation.<sup>[18]</sup> DRC analysis (Figure 8c) shows that the conversion of HCOOH\* to CH<sub>2</sub>O\*<sup>#</sup> (R11), the most difficult reaction step of the formate pathway, is also the rate-determining step. This result demonstrates that formate pathway dominates over RWGS pathway for the CO<sub>2</sub> hydrogenation to CH<sub>3</sub>OH on the surface of Cd/TiO<sub>2</sub> catalyst. In addition, it was found that the H<sub>2</sub> dissociation reaction step (R1 in Table 1) has only a minor influence on the overall reaction rate. The effect of H<sub>2</sub> and CO<sub>2</sub> partial pressure on the reaction rate is also investigated by MKM, as shown in Figure 8d. These results indicate that increasing H<sub>2</sub> partial pressure can enhance significantly the methanol production rate, which, in turn, is not affected by the CO<sub>2</sub> partial pressure.

## Conclusion

In conclusion, the reaction mechanisms of CO<sub>2</sub> hydrogenation to methanol by H<sub>2</sub> have been investigated in this study by comprehensive DFT and MKM. It is proposed that the interface between the Cd<sub>4</sub> cluster and the support of TiO<sub>2</sub> plays a key role for H<sub>2</sub> dissociation as well as preactivation of CO<sub>2</sub>. H<sub>2</sub> dissociation and CO<sub>2</sub> activation are energetically more favorable at the Cd-TiO<sub>2</sub> interface than that at bare TiO<sub>2</sub> surface and Cd cluster. Both CO<sub>2</sub> hydrogenation reactions to formate and CO are remarkably facilitated by the synergy between H<sup>-</sup> on Cd and H<sup>+</sup> on TiO<sub>2</sub> surface (Figure 3, formate pathway; Figure 4, RWGS pathway). In contrast, CO<sub>2</sub> conversion to CH<sub>3</sub>OH on bare TiO<sub>2</sub> is very difficult compared to the Cd/TiO<sub>2</sub> interface. Cd-TiO<sub>2</sub> interface is crucial for stabilizing various reaction intermediates and promoting the rate-determining step of formaldehyde formation identified by DFT and MKM. All these mechanism results indicates that the multifunctionality of Cd/TiO<sub>2</sub> interface including Lewis acids of metals and Lewis base of surface oxygen is of great importance accounting for the outstanding catalytic activity of Cd/TiO<sub>2</sub> material. Water molecules produced from the reaction or present in the reaction system can dramatically facilitate the most difficult reaction steps of RWGS reaction. However, formate is identified to be the relevant

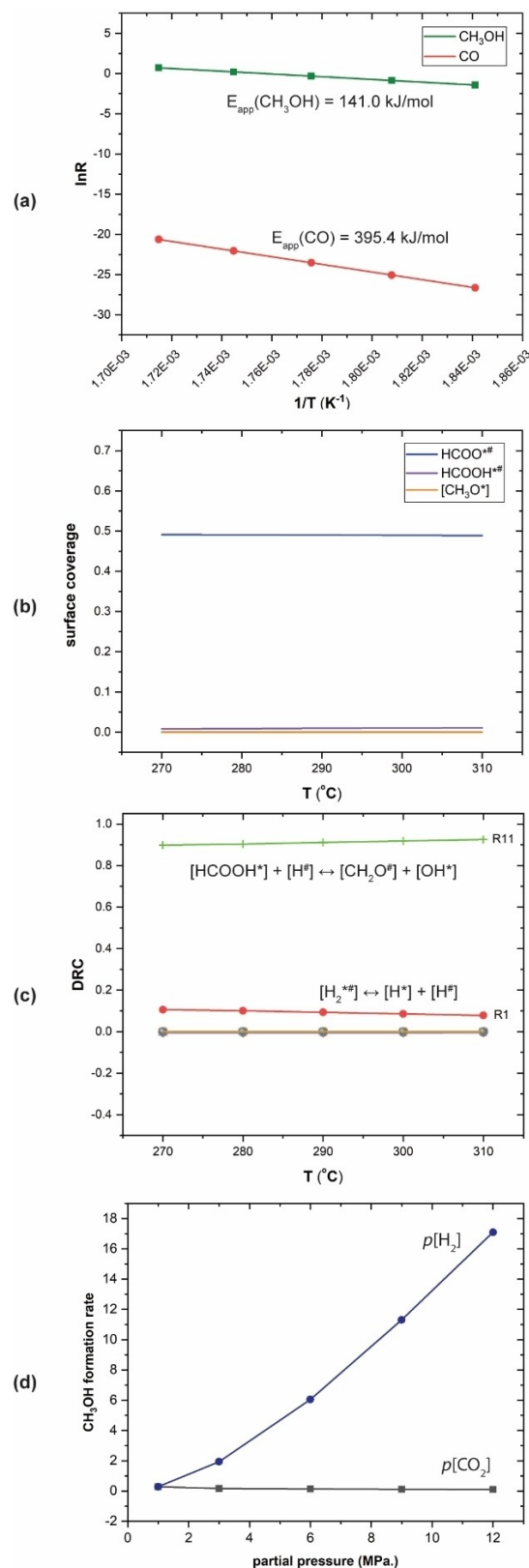


Table 1. Summary of elementary reaction steps and activation energies from DFT calculations used for microkinetic modeling. $E_{a-f}$ and $E_{a-b}$ are activation energy for forward and backward reaction, respectively. * and # represent $\text{TiO}_2$ and Cd sites on $\text{Cd}_x/\text{TiO}_2$ catalyst.		
Elementary reaction step	$E_{a-f}$ [eV]	$E_{a-b}$ [eV]
<b>H<sub>2</sub> dissociation</b>		
R0: $[\text{H}_2] + [*] + [\ddagger] \leftrightarrow [\text{H}_2^{*\ddagger}]$	0.00	0.02
R1: $[\text{H}_2^{*\ddagger}] \leftrightarrow [\text{H}^*] + [\text{H}^\ddagger]$	0.39	0.38
R2: $[\text{H}^\ddagger] + [*] \leftrightarrow [\text{H}^*] + [\ddagger]$	0.71	0.78
<b>Formate pathway 1 (<math>\text{CO}_2</math> to <math>\text{HCOOH}</math>)</b>		
R3: $[\text{CO}_2] + [\text{H}^*] + [\text{H}^\ddagger] \leftrightarrow [\text{CO}_2\text{-H}^*\text{H}^\ddagger]$	0.00	0.01
R4: $[\text{CO}_2\text{-H}^*\text{H}^\ddagger] \leftrightarrow [\text{HCOOH}^*] + [\ddagger]$	0.15	0.49
R5: $[\text{CO}_2] + [*] + [\text{H}^\ddagger] \leftrightarrow [\text{CO}_2^*\text{H}^\ddagger]$	0.00	0.14
R6: $[\text{CO}_2^*\text{H}^\ddagger] \leftrightarrow [\text{HCOO}^*] + [\ddagger]$	0.26	0.35
R7: $[\text{HCOO}^*] + [\text{H}^*] \leftrightarrow [\text{HCOOH}^*] + [*]$	0.22	0.34
R8: $[\text{HCOO}^*] + [\ddagger] \leftrightarrow [\text{HCOO}^{*\ddagger}]$	0.00	1.04
R9: $[\text{HCOO}^{*\ddagger}] + [\text{H}^*] \leftrightarrow [\text{HCOOH}^{*\ddagger}] + [*]$	0.41	0.12
R10: $[\text{HCOOH}^{*\ddagger}] \leftrightarrow [\text{HCOOH}^*] + [\ddagger]$	0.63	0.00
<b>Formate pathway 2 (<math>\text{HCOOH}</math> to <math>\text{CH}_2\text{O}</math>)</b>		
R11: $[\text{HCOOH}^*] + [\text{H}^\ddagger] \leftrightarrow [\text{CH}_2\text{O}^*] + [\text{OH}^*]$	0.65	0.33
R12: $[\text{CH}_2\text{O}^*] + [*] \leftrightarrow [\text{CH}_2\text{O}^*] + [\ddagger]$	0.00	0.44
R13: $[\text{OH}^*] + [\text{H}^*] \leftrightarrow [\text{H}_2\text{O}^*] + [*]$	0.18	0.63
R14: $[\text{H}_2\text{O}^*] + [\ddagger] \leftrightarrow [\text{H}_2\text{O}^*\ddagger]$	0.00	0.57
<b><math>\text{CH}_3\text{OH}</math> formation (<math>\text{CH}_2\text{O}</math> to <math>\text{CH}_3\text{OH}</math>)</b>		
R15: $[\text{CH}_2\text{O}^*] + [\text{H}^\ddagger] \leftrightarrow [\text{CH}_3\text{O}^*] + [\ddagger]$	0.00	1.40
R16: $[\text{CH}_3\text{O}^*] + [\text{H}^*] + [\ddagger] \leftrightarrow [\text{CH}_3\text{OH}^*] + [*]$	0.48	0.61
R17: $[\text{CH}_3\text{OH}^*] + [*] + [\ddagger] \leftrightarrow [\text{CH}_3\text{OH}^{*\ddagger}]$	0.00	0.73
<b>RWGS pathway 1 (<math>\text{CO}_2</math> to <math>\text{CO}</math>)</b>		
R18: $[\text{H}_2\text{O}] + [\text{H}^*] \leftrightarrow [\text{H}_2\text{O-H}^*]$	0.00	0.26
R19: $[\text{CO}_2] + [\text{H}_2\text{O-H}^*] \leftrightarrow [\text{CO}_2\text{-H}_2\text{O-H}^*]$	0.00	0.06
R20: $[\text{CO}_2\text{-H}_2\text{O-H}^*] + [\ddagger] \leftrightarrow [\text{HOCO}^*] + [\text{HOH}^*]$	0.42	0.37
R21: $[\text{H}_2\text{O}] + [*] \leftrightarrow [\text{HOH}^*]$	0.00	0.19
R22: $[\text{HOCO}^*] + [\text{H}^*] \leftrightarrow [\text{CO}^\ddagger] + [\text{HOH}^*]$	0.35	0.20
R23: $[\text{CO}] + [\ddagger] \leftrightarrow [\text{CO}^\ddagger]$	0.00	0.13
<b>RWGS pathway 2 (<math>\text{CO}</math> to <math>\text{CH}_2\text{O}</math>)</b>		
R24: $[\text{CO}] + [*] \leftrightarrow [\text{CO}^*]$	0.00	0.03
R25: $[\text{CO}^*] + [\text{H}^\ddagger] \leftrightarrow [\text{HCO}^{\#\ddagger}]$	0.32	0.77
R26: $[\text{HCO}^{\#\ddagger}] + [\text{H}_2] \leftrightarrow [\text{HCO}^{\#\ddagger}\text{-H}_2]$	0.00	0.01
R27: $[\text{HCO}^{\#\ddagger}\text{-H}_2] \leftrightarrow [\text{CH}_2\text{O}^*] + [\text{H}^\ddagger]$	1.10	1.67
<b><math>\text{CH}_3\text{O}^*</math> hydrogenolysis to <math>\text{CH}_3\text{OH}</math></b>		
R28: $[\text{CH}_3\text{O}^*] + [\text{H}_2] + [\ddagger] \leftrightarrow [\text{CH}_3\text{OH}^*] + [\text{H}^\ddagger]$	0.44	0.34
R29: $[\text{CH}_3\text{OH}^*] + [*] \leftrightarrow [\text{CH}_3\text{OH}^*]$	0.00	0.46

intermediate for  $\text{CO}_2$  hydrogenation to methanol, with formaldehyde formation being the rate-limiting reaction step. Our results demonstrate that  $\text{Cd}/\text{TiO}_2$  can be a promising candidate for valorization of  $\text{CO}_2$  to produce methanol and the multifunctionality of the metal-support interface is a crucial aspect for rational design of  $\text{CO}_2$  hydrogenation catalyst.

## Experimental Section

All DFT calculations have been performed using the Vienna Ab Initio Simulation Package (VASP).<sup>[19]</sup> The generalized gradient approximation (GGA) with PBE exchange and correlation functional was used to account for the exchange-correlation energy.<sup>[19b,20]</sup> The kinetic energy cutoff of the plane wave basis set was set to 400 eV. The threshold for energy convergence for each iteration was set to  $10^{-5}$  eV. Geometries were assumed to be converged when forces on each atom were less than 0.05 eV/Å. Gaussian smearing of the



**Figure 8.** Results of the microkinetic modeling for the  $\text{CO}_2$  hydrogenation on  $\text{Cd}/\text{TiO}_2$  catalyst. (a) is product formation rates as a function of temperature ( $T = 270\text{--}310^\circ\text{C}$ ) and the calculated apparent activation energy ( $E_{app}$ ). (b) is surface coverages of major surface intermediates at  $270\text{--}310^\circ\text{C}$ . (c) is degree of rate control analysis at  $270\text{--}310^\circ\text{C}$ . (d) is the partial pressure dependence of the  $\text{CH}_3\text{OH}$  formation rate at  $290^\circ\text{C}$ . The partial pressure of another reactant is fixed as 1 MPa.

population of partial occupancies with a width of 0.10 eV was used during iterative diagonalization of the Kohn-Sham Hamiltonian. The bulky TiO<sub>2</sub> unit cell in the phase of anatase was firstly fully optimized. The optimized lattice vectors of  $a=3.799 \text{ \AA}$   $b=3.799 \text{ \AA}$   $c=9.716 \text{ \AA}$  have a good agreement with the experiment parameters.<sup>[21]</sup> For Cd<sub>4</sub>/TiO<sub>2</sub> model, 1x3 and 2x4 supercells of anatase TiO<sub>2</sub> (101) surface with a vacuum space of 15 Å were built for investigation of the reaction mechanism of H<sub>2</sub> dissociation and CO<sub>2</sub> hydrogenation, respectively. These slab models contain six titanium layers with the bottom three layers were fixed while the rest was allowed to relax during the geometry optimization. The lattice parameters were fixed throughout the surface calculations. The nudged-elastic band method with the improved tangent estimate (CI-NEB) was used to determine the minimum energy path and to locate the transition state structure for each elementary reaction step.<sup>[22]</sup> The maximum energy geometry along the reaction path generated by the NEB method was further optimized using a quasi-Newton algorithm. In this procedure, only the extra-framework atoms were relaxed. Vibrational frequencies were calculated by determining the second derivatives of the Hessian matrix using the density functional perturbation theory as implemented in VASP 5.3.5. Transition state was confirmed by showing a single imaginary frequency corresponding to each reaction coordinate. Bader charge analysis was visualized by VESTA software.<sup>[23]</sup>

Mean-field microkinetic modeling (MKM) is applied based on the DFT calculations of all elementary reaction steps. The rate constant of the adsorption reaction is calculated by the Hertz-Knudsen equation [Eq. (1)].<sup>[24]</sup>

$$k_{ads} = \frac{PA}{\sqrt{2\pi mk_b T}} S \quad (1)$$

where  $k_{ads}$  is the rate constant of adsorption reaction,  $P$  is the partial pressure of the adsorbate in the gas phase,  $A$  is the surface area of the adsorption site,  $m$  is the mass of adsorbate,  $k_b$  is the Boltzmann constant,  $T$  is the temperature, and  $S$  is the sticking coefficient.

The desorption reaction is calculated by Equation (2):

$$k_{des} = \frac{k_b T^3 A (2\pi mk_b)}{h^3 \sigma \theta_{rot}} e^{\left(\frac{-E_{des}}{k_b T}\right)} \quad (2)$$

where  $k_{des}$  is the rate constant of desorption reaction,  $h$  is the Planck's constant,  $\sigma$  is the symmetry number of a molecule,  $\theta_{rot}$  is the rotational temperature of a molecule, and  $E_{des}$  is the desorption energy.

For the surface reaction, it is calculated by the Eyring equation [Eq. (3)].<sup>[25]</sup>

$$k = \frac{k_b T}{h} e^{-\frac{E_a}{RT}} \quad (3)$$

where  $k$  is the rate constant of surface reaction,  $E_a$  is the activation energy, and  $R$  is the gas constant.

The approach to MKM has been presented in detail elsewhere.<sup>[26]</sup> The differential equations are constructed using the rate constants and the set of elementary reaction steps. For each of the  $M$  components in the kinetic network, a single differential equation is in the form [Eq. (4)]:

$$r_i = \sum_{j=1}^N \left( k_j v_i^j \prod_{k=1}^M c_k^{v_k^j} \right) \quad (4)$$

where  $r_i$  is the rate reaction,  $k_j$  is the elementary reaction constant,  $v_i^j$  is the stoichiometric coefficient of component  $i$  in elementary reaction step  $k$  and  $c_k$  is the concentration of component  $k$  on the catalytic surface.

The degree of rate control (DRC) was performed to investigate the elementary steps that contribute to the rate control over the overall reaction ref: [21–23].<sup>[27]</sup> For elementary step  $i$ , the degree of rate control  $X_{RC,i}$  is defined as [Eq. (5)]

$$X_{RC,i} = \frac{k_i}{r} \left( \frac{\partial r}{\partial k_i} \right)_{k_{j \neq i, K_i}} = \left( \frac{\partial \ln r}{\partial \ln k_i} \right)_{k_{j \neq i, K_i}} \quad (5)$$

where  $k_i$ ,  $K_i$  and  $r$  are the rate constants, the equilibrium constant for step  $i$  and the reaction rate, respectively. All MKM results are simulated by a homemade script.

## Acknowledgments

Authors acknowledge financial support from the European Research Council (ERC) under the European Union's Horizon 2020 research and innovation programme (grant agreement No. 725686) J. M. gratefully acknowledges the Royal Thai Government Scholarships for the financial support. The use of super-computer facilities was sponsored by NWO Domain Science. The authors thank the Netherlands Organization for Scientific Research (NWO) for the access to SURFsara computational facilities and Dr. Dapeng Sun from Supermicro for valuable discussions about the MKM modeling.

## Conflict of Interest

The authors declare no conflict of interest.

## Data Availability Statement

The data that support the findings of this study are available in the supplementary material of this article.

**Keywords:** CO<sub>2</sub> · hydrogenation · CH<sub>3</sub>OH · Cd<sub>4</sub>/TiO<sub>2</sub> · multifunctional interface

- [1] a) W. Wang, S. Wang, X. Ma, J. Gong, *Chem. Soc. Rev.* **2011**, *40*, 3703–3727; b) A. Alvarez, A. Bansode, A. Urakawa, A. V. Bavykina, T. A. Wezendonk, M. Makkee, J. Gascon, F. Kapteijn, *Chem. Rev.* **2017**, *117*, 9804–9838.
- [2] M. Pérez-Fortes, J. C. Schöneberger, A. Boulamanti, E. Tzimas, *Appl. Energy* **2016**, *161*, 718–732.
- [3] a) W. Li, H. Wang, X. Jiang, J. Zhu, Z. Liu, X. Guo, C. Song, *RSC Adv.* **2018**, *8*, 7651–7669; b) R.-P. Ye, W. G. Jie Ding, M. D. Argyle, Q. Zhong, Y. Wang, C. K. Russell, Z. Xu, A. G. Russell, Q. Li, M. Fan, Y.-G. Yao, *Nat. Commun.* **2019**, *10*, 5698.

- [4] K. Ghasemzadeh, S. M. Sadati Tilebon, M. Nasirinezhad, A. Basile, in *Methanol*, **2018**, pp. 613–632.
- [5] J. Albo, M. Alvarez-Guerra, P. Castaño, A. Irabien, *Green Chem.* **2015**, *17*, 2304–2324.
- [6] a) W. Yang, K. Dastafkan, C. Jia, C. Zhao, *Advanced Materials Technologies* **2018**, *3*; b) J. Qiao, Y. Liu, F. Hong, J. Zhang, *Chem. Soc. Rev.* **2014**, *43*, 631–675; c) B. Khezri, A. C. Fisher, M. Pumera, *J. Mater. Chem. A* **2017**, *5*, 8230–8246; d) Z. Sun, T. Ma, H. Tao, Q. Fan, B. Han, *Chem* **2017**, *3*, 560–587.
- [7] a) M. Behrens, F. Studt, I. Kasatkin, S. Kühl, M. Hävecker, F. Abild-Pedersen, S. Zander, F. Girgsdies, P. Kurr, B.-L. Kniep, M. Tovar, R. W. Fischer, J. K. Nørskov, R. Schlögl, *Science* **2012**, *336*, 893–897; b) S. Kattel, P. J. Ramírez, J. G. Chen, J. A. Rodriguez, P. Liu, *Science* **2017**, *355*, 1296–1299.
- [8] a) J. Wu, M. Saito, M. Takeuchi, T. Watanabe, *Appl. Catal. A* **2001**, *218*, 235–240; b) X. Hu, W. Qin, Q. Guan, W. Li, *ChemCatChem* **2018**, *10*, 4438–4449.
- [9] a) K. Larmier, W. C. Liao, S. Tada, E. Lam, R. Verel, A. Bansode, A. Urakawa, A. Comas-Vives, C. Coperet, *Angew. Chem. Int. Ed. Engl.* **2017**, *56*, 2318–2323; b) S. Kattel, B. Yan, Y. Yang, J. G. Chen, P. Liu, *J. Am. Chem. Soc.* **2016**, *138*, 12440–12450.
- [10] J. Graciani, K. Mudiyansele, F. Xu, A. E. Baber, J. Evans, S. D. Senanayake, D. J. Stacchiola, P. L. Hrbek, J. F. Sanz, J. A. Rodriguez, *Science* **2014**, *345*, 546–550.
- [11] a) A. Vourros, I. Garagounis, V. Kyriakou, S. A. C. Carabineiro, F. J. Maldonado-Hódar, G. E. Marnellos, M. Konsolakis, *J. CO<sub>2</sub> Util.* **2017**, *19*, 247–256; b) Y. Hartadi, D. Widmann, R. J. Behm, *J. Catal.* **2016**, *333*, 238–250; c) J. A. Rodriguez, J. Evans, L. Feria, A. B. Vidal, P. Liu, K. Nakamura, F. Illas, *J. Catal.* **2013**, *307*, 162–169.
- [12] a) A. S. Malik, S. F. Zaman, A. A. Al-Zahrani, M. A. Daous, H. Driss, L. A. Petrov, *Appl. Catal. A* **2018**, *560*, 42–53; b) J. L. Snider, V. Streibel, M. A. Hubert, T. S. Choksi, E. Valle, D. C. Upham, J. Schumann, M. S. Duyar, A. Gallo, F. Abild-Pedersen, T. F. Jaramillo, *ACS Catal.* **2019**, *9*, 3399–3412; c) D. Wu, K. Deng, B. Hu, Q. Lu, G. Liu, X. Hong, *ChemCatChem* **2019**, *11*, 1598–1601; d) F. Jiang, S. Wang, B. Liu, J. Liu, L. Wang, Y. Xiao, Y. Xu, X. Liu, *ACS Catal.* **2020**, *10*, 11493–11509.
- [13] K. W. Ting, T. Toyao, S. M. A. H. Siddiki, K.-i. Shimizu, *ACS Catal.* **2019**, *9*, 3685–3693.
- [14] J. Wang, G. Li, Z. Li, C. Tang, Z. Feng, H. An, H. Liu, T. Liu, C. Li, *Sci. Adv.* **2017**, *3*, e1701290.
- [15] a) C. Yang, C. Pei, R. Luo, S. Liu, Y. Wang, Z. Wang, Z.-J. Zhao, J. Gong, *J. Am. Chem. Soc.* **2020**, *142*, 19523–19531; b) S. Dang, B. Qin, Y. Yang, H. Wang, J. Cai, Y. Han, S. Li, P. Gao, Y. Sun, *Sci. Adv.* **2020**, *6*, eaaz2060.
- [16] a) Y. Li, S. H. Chan, Q. Sun, *Nanoscale* **2015**, *7*, 8663–8683; b) S. Kattel, P. Liu, J. G. Chen, *J. Am. Chem. Soc.* **2017**, *139*, 9739–9754.
- [17] a) M. Dou, M. Zhang, Y. Chen, Y. Yu, *Surf. Sci.* **2018**, *672–673*, 7–12; b) J. Wang, G. Li, Z. Li, C. Tang, Z. Feng, H. An, H. Liu, T. Liu, C. Li, *Sci. Adv.* **2018**, *3*, e1701290; c) J. Ye, C. Liu, D. Mei, Q. Ge, *ACS Catal.* **2013**, *3*, 1296–1306; d) C. Liu, B. Yang, E. Tyo, S. Seifert, J. DeBartolo, B. von Issendorff, P. Zapol, S. Vajda, L. A. Curtiss, *J. Am. Chem. Soc.* **2015**, *137*, 8676–8679.
- [18] J. Wang, J. Meeprasert, Z. Han, H. Wang, Z. Feng, C. Tang, F. Sha, S. Tang, G. Li, C. L. E. A. Pidko, *Chin. J. Catal.* **2021**, *42*.
- [19] a) G. Kresse, J. Furthmüller, *Comput. Mater. Sci.* **1996**, *6*, 15–50; b) G. Kresse, J. Furthmüller, *Phys. Rev. B* **1996**, *54*, 11169–11186.
- [20] J. P. Perdew, K. Burke, M. Ernzerhof, *Phys. Rev. Lett.* **1996**, *77*, 3865–3868.
- [21] U. Diebold, *Surf. Sci. Rep.* **2003**, *48*, 53–229.
- [22] G. Henkelman, B. P. Uberuaga, H. Jónsson, *J. Chem. Phys.* **2000**, *113*, 9901–9904.
- [23] K. Momma, F. Izumi, *J. Appl. Crystallogr.* **2011**, *44*, 1272–1276.
- [24] P. Nitoń, A. Żywociński, M. Fiałkowska, R. Hołyst, *Nanoscale* **2013**, *5*, 9732–9738.
- [25] H. Eyring, *J. Chem. Phys.* **1935**, *3*, 107.
- [26] a) I. A. W. Filot, R. A. v. Santen, E. J. M. Hensen, *Angew. Chem. Int. Ed.* **2014**, *53*, 12746–12750; *Angew. Chem.* **2014**, *126*, 12960–12964; b) I. A. W. Filot, R. J. P. Broos, J. P. M. v. Rijn, G. J. H. A. v. Heugten, R. A. v. Santen, E. J. M. Hensen, *ACS Catal.* **2015**, *5*, 5453–5467; c) J.-X. Liu, Y. Su, I. A. W. Filot, E. J. M. Hensen, *J. Am. Chem. Soc.* **2018**, *140*, 4580–4587.
- [27] a) C. T. Campbell, *Top. Catal.* **1994**, *1*, 353–366 ; b) C. T. Campbell, *J. Catal.* **2001**, *204*, 520–524; c) C. Stegelmann, A. Andreasen, C. T. Campbell, *J. Am. Chem. Soc.* **2009**, *131*, 8077–8082.
- [28] J. Zhao, *Phys. Rev. A* **2001**, *64*, 043204.
- [29] a) M. Boronat, F. Illas, A. Corma, *J. Phys. Chem. A* **2009**, *113*, 3750–3757; b) W. Wan, X. Nie, M. J. Janik, C. Song, X. Guo, *J. Phys. Chem. C* **2018**, *122*, 17895–17916; c) K. Sun, M. Kohyama, S. Tanaka, S. Takeda, *J. Phys. Chem. C* **2014**, *118*, 1611–1617.
- [30] G. Hu, Z. Wu, D.-e. Jiang, *J. Phys. Chem. C* **2018**, *122*, 20323–20328.

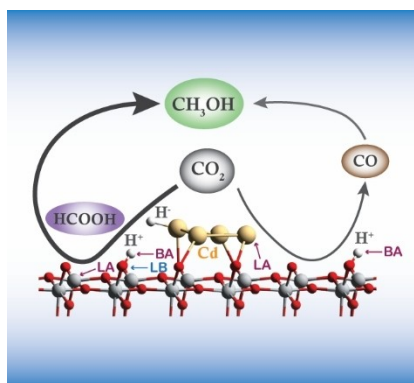
Manuscript received: October 29, 2021

Revised manuscript received: December 12, 2021

Version of record online: ■■■, ■■■■

## RESEARCH ARTICLE

**Multifunctional catalysts:** The detailed reaction mechanism of  $\text{CO}_2$  hydrogenation to  $\text{CH}_3\text{OH}$  was investigated over the multifunctional catalyst of  $\text{Cd}_4/\text{TiO}_2$ . Benefiting from the cooperation between Lewis acids from the Cd and Ti sites and Lewis bases from  $\text{TiO}_2$  surface oxygen atoms, the  $\text{Cd}_4/\text{TiO}_2$  exhibited high activity and selectivity for the  $\text{CH}_3\text{OH}$  production.



*Dr. G. Li\*, J. Meeprasert, Prof. J. Wang,  
Prof. C. Li, Prof. E. A. Pidko\**

1 – 11

**$\text{CO}_2$  Hydrogenation to Methanol  
over  $\text{Cd}_4/\text{TiO}_2$  Catalyst: Insight into  
Multifunctional Interface**

